



LAWRENCE
LIVERMORE
NATIONAL
LABORATORY

An Unsplit, Cell-Centered Godunov Method for Ideal MHD

R. Fisher, R. Crockett, P. Colella, R. Klein, C.
McKee

October 17, 2003

Journal of Computational Physics

Disclaimer

This document was prepared as an account of work sponsored by an agency of the United States Government. Neither the United States Government nor the University of California nor any of their employees, makes any warranty, express or implied, or assumes any legal liability or responsibility for the accuracy, completeness, or usefulness of any information, apparatus, product, or process disclosed, or represents that its use would not infringe privately owned rights. Reference herein to any specific commercial product, process, or service by trade name, trademark, manufacturer, or otherwise, does not necessarily constitute or imply its endorsement, recommendation, or favoring by the United States Government or the University of California. The views and opinions of authors expressed herein do not necessarily state or reflect those of the United States Government or the University of California, and shall not be used for advertising or product endorsement purposes.

An Unsplit, Cell-Centered Godunov Method for Ideal MHD

Robert K. Crockett ^{a,*} Phillip Colella ^c Robert T. Fisher ^d
Richard I. Klein ^{b,d} Christopher F. McKee ^{a,b}

^a*Physics Department, University of California, Berkeley, CA 94720, USA*

^b*Astronomy Department, University of California, Berkeley, CA 94720, USA*

^c*Lawrence Berkeley National Laboratory, Berkeley CA, 94720, USA*

^d*Lawrence Livermore National Laboratory, Livermore CA, 94551, USA*

Received 29 August 2003

Abstract

We present a second-order Godunov algorithm for multidimensional, ideal MHD. Our algorithm is based on the unsplit formulation of Colella (J. Comput. Phys. vol. 87 (1990)), with all of the primary dependent variables centered at the same location. To properly represent the divergence-free condition of the magnetic fields, we apply a discrete projection to the intermediate values of the field at cell faces, and apply a filter to the primary dependent variables at the end of each time step. We apply the method to a suite of linear and nonlinear tests to ascertain accuracy and stability of the scheme under a variety of conditions. The test suite includes rotated planar linear waves, MHD shock tube problems, and low-beta flux tubes. For all of these cases, we observe that the algorithm is second-order accurate for smooth solutions, converges to the correct weak solution for problems involving shocks, and exhibits no evidence of instability or loss of accuracy due to the possible presence of non-solenoidal fields.

Key words: magnetohydrodynamics, numerical approximation, stability and convergence of difference schemes,

PACS:

* Corresponding author.

Email address: mookie@astron.berkeley.edu (Robert K. Crockett).

URL: astron.berkeley.edu/~mookie/ (Robert K. Crockett).

1 Introduction

In this paper we present a new Godunov method for the equations of multidimensional ideal magnetohydrodynamics (MHD). We give the first published results from an implementation of an unsplit method for these equations. The unsplit algorithm follows that of Colella [9]. The base scheme solves the ideal MHD equations using a second-order predictor-corrector formalism. To the base scheme we add three algorithmic components, new in the context of MHD, and measure their effects upon accuracy and stability. The first component is a MAC projection [5,17] step, which uses a Poisson solver to ensure that the cell-edge centered fields used to calculate fluxes are divergence-free to machine precision. The second is an approximate projection that uses the same Poisson solver to ensure that the cell-centered field is divergence-free to second-order. The last component is a filter that also acts to suppress monopole sources in the cell-centered field. The use of MAC and approximate projections along with filtering techniques to enforce the divergence-free constraint, $\nabla \cdot \vec{B} = 0$, is novel in the context of ideal MHD simulations.

The section that follows covers recent work and some of the schemes used for ideal MHD simulation. It also introduces methods for enforcing the divergence-free constraint, and introduces some issues surrounding multidimensional MHD. Section 3 introduces our basic algorithm and the extensions we have implemented. A suite of linear and nonlinear test problems will be used to determine which of our algorithmic extensions are best suited to each problem type. These tests and results are covered in Section 4. The overall purpose is to find one combination of these extensions which is well suited to all of the problems considered. This will be done through comparisons to published results and in some cases to a divergence-wave (or eight-wave) MHD algorithm we have implemented.

2 Background

The study of numerical algorithms for magnetohydrodynamics simulations remains an active one, with no one method having become the standard. Two generic algorithms are the most widely used at present: the Method of Characteristics/Constrained Transport (MOC/CT) [13,26] and shock-capturing (Godunov) methods [8,31,11,4]. Each has distinct benefits and drawbacks. Codes implementing the MOC/CT algorithm are relatively simple in design, and satisfy the divergence-free constraint to machine precision. However, method of characteristics used by the ZEUS scheme, as outlined in [26], is by construction second-order on Alfvén and advective waves, but does not address the two compressive waves of ideal MHD. Moreover, Falle [14] found that ZEUS

exhibits spurious rarefaction shocks in certain 1-D MHD shock tubes for a non-isothermal equation of state. Codes implementing the shock-capturing algorithm on the other hand, while more complex, give highly accurate results even for strong shocks. They suffer from the drawback that the divergence-free constraint is only satisfied to truncation error, which can be large in the region of large jumps. In order to treat this difficulty, a variety of techniques have come into use. One such is the hybrid CT/shock-capturing scheme [4,24], for which the constraint is satisfied by design like in the MOC/CT case. The cost to the accuracy of the underlying shock-capturing scheme is unclear. Another approach, originally due to Brackbill and Barnes [7] and implemented by workers such as Ryu et al [23], uses a divergence cleaning step on the cell-centered fields to enforce the constraint. In a third approach, Gombosi et al [16] use an 8-wave (or divergence-wave) reformulation of the ideal MHD equations originally due to Godunov [15]. Tóth [29] (hereafter T00) implements all three types of schemes, among others, using them as the basis for a comparison on a variety of 1-D and 2-D tests. More recently, Dedner et al [12] compare several hyperbolic schemes with additional waves and divergence-damping terms on the T00 tests.

The 2-D tests of T00 serve to underscore the importance of using multidimensional problems in evaluating different algorithms, since it was mainly in this context that differences between them became apparent. This is to be expected, since errors due to non-solenoidal fields will generally only show up for problems in two or more dimensions. All the aforementioned shock-capturing MHD schemes use the same operator-split (or dimensionally-split) formalism to treat multidimensional ideal MHD. This means that, for each spatial dimension of the scheme, the one dimensional MHD equations are applied once. Unsplit schemes, which use instead the full multidimensional version of the equations, have been implemented and shown to give results equivalent to those of split methods for hydrodynamical problems [9]. No such scheme for ideal MHD has appeared in the literature to date. Nor, therefore, has the efficacy of different approaches for enforcing the divergence-free constraint in unsplit schemes been explored.

2.1 *The Divergence-free Constraint*

Some means must be employed to ensure that the field satisfies the divergence-free constraint, since this is only guaranteed to within truncation error in shock-capturing schemes. In the region of large jumps in the field, these truncation errors can lead to $\mathcal{O}(1)$ solution errors and incorrect dynamics, such as fluid accelerations parallel to the magnetic field lines. The different techniques for addressing this problem mentioned above each have their own strengths and weaknesses.

The divergence-wave MHD algorithm, as implemented by Gombosi et al [16] and others, addresses the problem by adding additional terms corresponding to monopoles to the ideal MHD equations. The resultant equations are symmetrizable, so that they are Galilean invariant and conserve $\nabla \cdot \vec{B}$ [15]. The additional terms show up in two ways for shock-capturing schemes. Since they modify the 1-D MHD equations used for characteristic tracing to include an additional eighth wave that travels at the flow speed, monopoles will be advected along with the flow. Such monopoles could be carried out of the domain, or they might build up at a stagnation point. Secondly, the additional terms appear as source terms, making the system non-conservative if the divergence-free condition isn't already satisfied. In Section 4.4 we show a situation in which such terms are negligible and conservation is only trivially violated.

Dedner et al [12] test a scheme that extends the divergence-wave concept to damp and advect monopole sources, even in stagnation points in the flow. This is done through the magnetic analog of an artificial compressibility term, an approach that surfaced earlier in the context of the Maxwell equations [20]. To the extent that the computed auxiliary field remains continuous, the scheme will remain divergence free. Any monopole sources will be advected at the fastest speed allowed under the Courant condition, and damped as they are advected. This method is very useful on unstructured grids, where solving the Poisson equation in order to project out the solenoidal component of the field is difficult.

Divergence cleaning, or Hodge projection, in shock-capturing schemes can address the problem of non-solenoidal fields in two ways. The most widely discussed [2,7,23] involves projection of the cell-centered field onto the space of divergence-free fields. Projecting in this manner with a centered difference approximation to the divergence is consistent with the underlying cell-centered scheme. One is left with fields at the advanced time which are divergence-free to machine accuracy. Such a projection has been found to give correct field topologies in shock tube problems [23]. On the other hand, changing the magnetic field affects energy balance in the fluid. A decrease in magnetic energy, for instance, might lead to an increase in internal energy, depending on how the projection is performed. Moreover, choosing to eliminate the divergence as measured in one metric probably does not guarantee that monopole effects are not entering into the dynamics. An illustrative example from incompressible flow [19] where an analogous constraint on the fluid velocity, $\nabla \cdot \vec{v} = 0$, occurs shows that in the case of a centered difference metric, checkerboard modes in the velocity can cause instabilities when using a centered difference to approximate the divergence. Such modes must be damped by a suitably chosen filter in order to regain stability.

Another option is to project the fields at cell-edges, which are then used to

calculate fluxes. In a MAC discretization [5,17], backward difference approximation to the divergence and a five-point finite difference Laplacian are used to enforce the divergence-free constraint to within machine precision. It has the added advantage that it does not affect the conservation properties of the scheme. It may be argued that this method for cleaning the fields is more consistent with Godunov-type schemes than a cell-centered approach because of this, and because it uses the same discretization of the divergence operator in calculating $\nabla \cdot \vec{B}$ as does the update in differencing the fluxes to calculate $\nabla \cdot \vec{F}$. Nonetheless, the extent to which such a projection is required in magnetohydrodynamic problems has remained unclear to this point.

2.2 Multidimensional MHD

The MHD equations in two or more dimensions are decidedly more complex to solve than in one dimension. In MHD simulations with variations along the x-axis alone, there is no change in the field along the x-axis. The divergence-free constraint is therefore trivially satisfied. Obtaining the solution to the Riemann problem upon which Godunov methods are based is also relatively straightforward in 1-D.

In multiple dimensions, we are solving the full equations of ideal MHD, which in conservation form are

$$\partial_t \rho + \nabla \cdot (\rho \vec{u}) = 0 \quad (1)$$

$$\partial_t(\rho \vec{u}) + \nabla \cdot \left[\rho \vec{u} \vec{u} + \left(P + \frac{B^2}{8\pi} \right) \mathbf{I} - \frac{1}{4\pi} \vec{B} \vec{B} \right] = 0 \quad (2)$$

$$\partial_t(\vec{B}) + \nabla \cdot [\vec{u} \vec{B} - \vec{B} \vec{u}] = 0 \quad (3)$$

$$\partial_t(\rho E) + \nabla \cdot \left[\left(\rho E + P + \frac{1}{8\pi} B^2 \right) \vec{u} - \frac{1}{4\pi} (\vec{u} \cdot \vec{B}) \vec{B} \right] = 0, \quad (4)$$

subject to the constraint $\nabla \cdot \vec{B} = 0$. Here ρ is the mass density, $\rho \vec{u}$ the momentum density, \vec{B} the magnetic field, and $\rho E = \frac{1}{2} \rho |\vec{u}|^2 + \frac{1}{8\pi} |\vec{B}|^2 + \frac{1}{\gamma-1} P$ the total energy density. The ∂_t notation denotes derivatives with respect to time. In 2-D MHD, for example, the full x-momentum equation is

$$\partial_t(\rho u) + \partial_x \left(\rho u^2 + P + \frac{-B_x^2 + B_y^2}{8\pi} \right) + \partial_y \left(\rho uv - \frac{B_x B_y}{4\pi} \right) = 0, \quad (5)$$

For the sake of simplicity, many codes use a dimensional-splitting approach to solve the multidimensional MHD equations. In this approach, the 1-D MHD equations are solved once for each direction. The 1-D equations applied in a split method for 2-D MHD are

$$\partial_t(\rho u) + \partial_x \left(\rho u^2 + P + \frac{B_y^2}{8\pi} \right) = 0 \quad (6)$$

$$\partial_t(\rho u) + \partial_y(\rho uv) - B_y \partial_y \left(\frac{B_x}{4\pi} \right) = 0. \quad (7)$$

Notice that terms involving derivatives of the normal field, like $-\frac{1}{4\pi} B_x \partial_x B_x$ in equation 5, are absent in equations 6 and 7 since the 1-D MHD equations exclude the possibility of jumps in the normal field. Such terms are absent in most MHD schemes using dimensional-splitting published to date. As a result, one would expect decreased accuracy on multidimensional problems. This shortcoming is absent in an unsplit method since, properly implemented, it uses the full 2-D equation (5).

3 Equations and Algorithms

In general for hyperbolic conservation laws, the conserved variables U evolve according to a conservation law $\partial_t U + \nabla \cdot \vec{F}(U) = 0$. Our code uses a second-order Godunov-type method for hyperbolic conservation laws [6]. Such volume-average schemes follow the flux of conserved quantities such as momentum into and out of each cell comprising the computational domain. Quantities are stored at cell-centers, their value at this point being the volume-average over the entire cell. During the course of a timestep, the flux of the conserved quantities at each edge of each cell is computed. Differencing these fluxes gives the update of the conserved quantity to the next time (see Figure 1).

More specifically, our code is based on the unsplit MHD algorithm of Colella [9]. It ostensibly tracks the evolution of the conserved density ρ , three components of momentum $\rho \vec{u}$, three components of magnetic field \vec{B} , and total energy density ρE , in two spatial dimensions. These variables would then be evolved according to the ideal MHD equations (1-4). However, for simplicity a set of primitive variables W consisting of the density, velocity, field, and pressure are evolved in time:

$$W = [\rho \ u \ v \ w \ B_x \ B_y \ B_z \ P]. \quad (8)$$

We will switch freely between U and W here depending on which is most convenient; the indices will indicate the centering of the variables. Thus i, j will denote cell-centered states, i, j, \pm forward- and backward-interpolations to cell-edges, and $i + \frac{1}{2}, j$ and $i, j + \frac{1}{2}$ (Riemann) states at the edges.

The fundamental aspects of our scheme are as follows. Given the state $W_{i,j}^n$ at time n and spatial coordinate (x_i, y_j) , we simultaneously interpolate in space

and extrapolate in time to obtain the states $\hat{W}_{i,j,\pm,x}^{n+\frac{1}{2}}$ on the two x-boundaries of each cell (i, j) . The same is done for the states at the y-boundaries, $\hat{W}_{i,j,\pm,y}^{n+\frac{1}{2}}$. This is done in the normal and transverse predictor steps of the algorithm. Next, the Riemann problem is solved using the $\hat{W}_{i,j,\pm,x}^{n+\frac{1}{2}}$ states. These Riemann states are used to calculate fluxes at each edge of a cell in the corrector step. The fluxes are then differenced to give the update to the next timestep, $W_{i,j}^{n+1}$. We go into more detail on these steps of our scheme in Sections 3.1 through 3.4.

The additional parts of our MHD scheme consist in part of additional terms in the normal predictor step to ensure correct multidimensional behavior, and several steps that address the divergence-free constraint. These are also discussed in Sections 3.1 through 3.4.

3.1 Normal Predictor

The predictor computes $W_{i,j,\pm,x}^{n+\frac{1}{2}}$ and $W_{i,j,\pm,y}^{n+\frac{1}{2}}$ using a Taylor series expansion:

$$W_{i,j,\pm,x}^{n+\frac{1}{2}} = W_{i,j}^n \pm \frac{\Delta x}{2} \partial_x W - \frac{\Delta t}{2} \mathbf{A}^x \partial_x W - \frac{\Delta t}{2} \partial_y F^y. \quad (9)$$

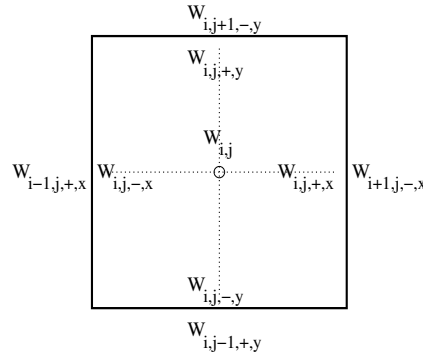


Fig. 1. Single cell of the computational domain, showing interpolated states $W_{i,j,\pm,x}^{n+\frac{1}{2}}$ and $W_{i,j,\pm,y}^{n+\frac{1}{2}}$, and cell-centered state $W_{i,j}$. The (Riemann) states at cell edges would lie between the interpolated states. So $W_{i+\frac{1}{2},j}^{n+\frac{1}{2}}$, for instance, would lie between $W_{i,j,+x}^{n+\frac{1}{2}}$ and $W_{i+1,j,-x}^{n+\frac{1}{2}}$.

Here the matrix \mathbf{A} is related to the flux F^x of the conserved variable U by $\mathbf{A} = (\partial_U W)(\partial_W F^x)$. We give formulas for $W_{i,j,\pm,x}^{n+\frac{1}{2}}$, those for $W_{i,j,\pm,y}^{n+\frac{1}{2}}$ being similar. The first three terms on the right-hand side are computed in the normal predictor, and we label this intermediate result $\hat{W}_{i,j,\pm,x}^{n+\frac{1}{2}}$. We now separate out the evolution of the normal field $B_n = B_x$ through the following notation:

$$\hat{W} = \begin{bmatrix} \tilde{W} \\ B_x \end{bmatrix}, \quad \mathbf{A} = \begin{bmatrix} \tilde{\mathbf{A}} & a_B \\ 0 & 0 \end{bmatrix}. \quad (10)$$

The matrix $\tilde{\mathbf{A}}$ corresponds to the usual 1-D MHD equations, with its seven characteristics: forward- and backward-propagating fast, slow, and Alfvén, plus the advective wave. Second-order accuracy is achieved in part through the use of characteristic analysis to calculate derivatives in the spatial interpolation. This characteristic interpolation is based on calculation of the eigenvalues λ_k and left- and right-eigenvectors l_k and r_k of the matrix $\tilde{\mathbf{A}}$, giving the following expression for the interpolation of the \tilde{W} variables to cell-edges:

$$\tilde{W}_{i,j,\pm,x}^{n+\frac{1}{2}} = \tilde{W}_{i,j}^n + \frac{1}{2} \sum_{k:\lambda_k \gtrless 0} \left(\pm 1 - \frac{\Delta t}{\Delta x} \lambda_k \right) \alpha_k r_k. \quad (11)$$

The α_k represent the strength of the k^{th} wave in the interpolant. The sum over $\lambda_k < 0$ would correspond to backward-propagating waves used in the interpolation to $\tilde{W}_{i,j,-,x}^{n+\frac{1}{2}}$, and similarly for $\lambda_k > 0$ and $\tilde{W}_{i,j,+,x}^{n+\frac{1}{2}}$.

A full accounting for all x-derivative terms in the 2-D MHD equations shows that a_B is given by

$$a_B = - \left[0, \frac{B_x}{4\pi\rho}, \frac{B_y}{4\pi\rho}, \frac{B_z}{4\pi\rho}, v, w, \frac{\vec{u} \cdot \vec{B}}{4\pi} \right]^T. \quad (12)$$

These terms are essential to the second-order accuracy of the scheme, in particular on multidimensional problems such as waves not propagating along cardinal axes. They are incorporated into our algorithm through a simple finite differencing of the normal derivative of the normal field, $\partial_n B_n = \partial_x B_x$. The terms are added to those already present due to the characteristics-based interpolation:

$$\tilde{W}_{i,j,\pm,x}^{n+\frac{1}{2}} = \tilde{W}_{i,j,\pm,x}^{n+\frac{1}{2}} - \frac{\Delta t}{2} a_B (\mathcal{D}_x^0 B_x^n)_{i,j}. \quad (13)$$

The $(\mathcal{D}_x^0 B_x^n)_{i,j} = ((B_x)_{i+1,j}^n - (B_x)_{i-1,j}^n)/(2\Delta x)$ in the last (correction) term is the centered-difference approximation to $\partial_x B_x$. The need for such correction terms in an unsplit scheme for multidimensional MHD was not addressed in C90. It was first noted by Stone [27] during an examination of the accuracy of an unsplit Godunov scheme on advected flux rings.

3.2 Transverse Predictor

The last term in the evolution equation (9) is included via the transverse predictor. The basic idea is to approximate transverse derivatives (in this case in the y-direction) using a 1-D Godunov method. We take the states calculated in the normal predictor, $\hat{W}_{i,j,\pm,y}^{n+\frac{1}{2}}$, and first use them to solve the Riemann problem at each y-boundary in the domain. The resulting Riemann states $U_{i,j+\frac{1}{2}}^{n+\frac{1}{2}}$ are subsequently used to calculate the fluxes needed for the last term in equation 9. In more mathematical terms,

$$U_{i,j+\frac{1}{2}}^{n+\frac{1}{2}} = \mathcal{R}\left(\hat{W}_{i,j,+,y}^{n+\frac{1}{2}}, \hat{W}_{i,j+1,-,y}^{n+\frac{1}{2}}\right) \quad (14)$$

$$F_{i,j+\frac{1}{2}}^{y,n+\frac{1}{2}} = F^y\left(U_{i,j+\frac{1}{2}}^{n+\frac{1}{2}}\right). \quad (15)$$

Here $\mathcal{R}(\cdot, \cdot)$ denotes the Riemann problem solution using the two states on either side of an edge as input; see Section 3.4. It is then a straightforward matter to use these fluxes to calculate a finite-difference approximation to $\partial_y F^y$, and thereby complete the calculation of the edge-centered states.

3.3 Corrector

The corrector first calculates fluxes at all cell-edges using another Riemann problem solve. At this stage, we have the first-order accurate approximation to the interpolated states $W_{i,j,\pm,\cdot}^{n+\frac{1}{2}}$ from the predictor in hand. The Riemann solver takes these states and returns a single state for each cell-edge, $U_{i+\frac{1}{2},j}^{n+\frac{1}{2}}$ and $U_{i,j+\frac{1}{2}}^{n+\frac{1}{2}}$. For instance,

$$U_{i+\frac{1}{2},j}^{n+\frac{1}{2}} = \mathcal{R}\left(W_{i,j,+,x}^{n+\frac{1}{2}}, W_{i+1,j,-,x}^{n+\frac{1}{2}}\right). \quad (16)$$

The formula for $U_{i,j+\frac{1}{2}}^{n+\frac{1}{2}}$ is similar. See Section 3.4 for more details on the Riemann problem solution.

The states at cell-edges are not guaranteed to be divergence-free. We modify the C90 algorithm to enforce the divergence-free condition for the Riemann problem states. These Riemann states have a non-solenoidal component that we treat through a MAC projection, earlier used in the context of incompressible fluid computations [5]. The edge-centered field \vec{B}^* is used to calculate a cell-centered monopole charge density $q_M = \nabla \cdot \vec{B}^*$, and a Poisson solver is in turn used to find the scalar field ϕ . This scalar field satisfies the following relations, in which \mathcal{D}_x^\pm correspond to the forward- and backward-difference approximations to the derivative $\frac{\partial}{\partial x}$, and similarly for \mathcal{D}_y^\pm :

$$(q_M)_{i,j} = \mathcal{D}_x^-(B_x^*)_{i+\frac{1}{2},j} + \mathcal{D}_y^-(B_y^*)_{i,j+\frac{1}{2}} \quad (17)$$

$$[\mathcal{D}_x^+ \mathcal{D}_x^- + \mathcal{D}_y^+ \mathcal{D}_y^-] \phi_{i,j} = (q_M)_{i,j}. \quad (18)$$

$$(19)$$

The correction to the field is calculated from ϕ as follows:

$$(B_x)_{i+\frac{1}{2},j} = (B_x^*)_{i+\frac{1}{2},j} - \mathcal{D}_x^+ \phi_{i,j} \quad (20)$$

$$(B_y)_{i+\frac{1}{2},j} = (B_y^*)_{i+\frac{1}{2},j} - \frac{1}{2} [\mathcal{D}_y^0 \phi_{i+1,j} + \mathcal{D}_y^0 \phi_{i,j}] \quad (21)$$

$$(B_x)_{i,j+\frac{1}{2}} = (B_x^*)_{i,j+\frac{1}{2}} - \frac{1}{2} [\mathcal{D}_x^0 \phi_{i,j+1} + \mathcal{D}_x^0 \phi_{i,j}] \quad (22)$$

$$(B_y)_{i,j+\frac{1}{2}} = (B_y^*)_{i,j+\frac{1}{2}} - \mathcal{D}_y^+ \phi_{i,j} \quad (23)$$

With this correction to the magnetic field of the Riemann states, the L^1 norm of the MAC monopole density is reduced from its initial value by a user-settable multiplicative factor, in our case 10^{-12} .

The algorithm now proceeds to calculate the fluxes associated with the Riemann states. These fluxes are then differenced to give the update to the next time $U_{i,j}^{n+1}$:

$$F_{i+\frac{1}{2},j}^{x,n+\frac{1}{2}} = F^x \left(U_{i+\frac{1}{2},j}^{n+\frac{1}{2}} \right) \quad (24)$$

$$U_{i,j}^{n+1} = U_{i,j}^n - \Delta t \mathcal{D}_x^- F_{i+\frac{1}{2},j}^{x,n+\frac{1}{2}} - \Delta t \mathcal{D}_y^- F_{i,j+\frac{1}{2}}^{y,n+\frac{1}{2}} \quad (25)$$

After the update to t^{n+1} , we are left with a cell-centered field $\vec{B}_{i,j}^{*,n+1}$ that is no longer divergence-free by a centered-difference divergence metric. To

what extent, if any, this is a problem depends on the physical problem being considered, and will be addressed later.

For those cases where a reduction of the divergence is required, two algorithmic extensions have been implemented. The first follows from noting that it is desirable to have a diffusive term of the form

$$\frac{\partial(\nabla \cdot \vec{B})}{\partial t} = \eta \nabla^2 (\nabla \cdot \vec{B}) \quad (26)$$

act on the divergence of \vec{B} . This may be rewritten to eliminate a spatial derivative by pulling out a divergence operator, giving

$$\frac{\partial \vec{B}}{\partial t} = \eta \nabla (\nabla \cdot \vec{B}) \quad (27)$$

A simple, single-step filter may be derived [21] as a finite-difference approximation of equation 27:

$$B_x := B_x + \eta \Delta t (\mathcal{D}_x^+ \mathcal{D}_x^- B_x + \mathcal{D}_x^0 \mathcal{D}_y^0 B_y) \quad (28)$$

$$B_y := B_y + \eta \Delta t (\mathcal{D}_x^0 \mathcal{D}_y^0 B_x + \mathcal{D}_y^+ \mathcal{D}_y^- B_y) \quad (29)$$

In order to choose a value for η we use Fourier stability analysis, giving a stability condition for the scheme in equations 28 and 29 of $\Delta t \leq \frac{2(\Delta x)^2}{5\eta}$. Since Δt is set by the Courant condition, we are able to derive a condition on η , giving the maximum amount of diffusion of the monopole sources possible, given our timestep and grid spacing:

$$\eta = C \frac{(\Delta x)^2}{\Delta t} \quad (30)$$

with $C \leq \frac{2}{5}$. A stronger condition, $C \leq \frac{1}{5}$, will always damp monopole modes. This formulation will both decrease the cell-centered divergence and damp checkerboard modes. Owing to the latter feature, this filtering method is always used when an approximate projection is performed.

The filter provides two means of modifying its numerical effect. The first is through the parameter C , for which we found, through the nonlinear tests outlined in Section 4, a value of 10^{-2} worked best. The second is whether the modified magnetic field also results in a changed total energy or merely a changed magnetic energy. If the filter is applied to the conserved variables U^{n+1} , then the changed magnetic field causes no change in the total energy. Any addition (subtraction) of magnetic energy shows up as a decrease (increase) in the internal energy. If it is applied after the updated conserved

variable state is converted back to primitive variables, however, then a change in total energy results. The internal energy in this case is not affected.

The second means for treating non-solenoidal cell-centered fields is an approximate projection, in which the cell-centered divergence is used to calculate a monopole charge density $q_M = \mathcal{D}_x^0 B_x^* + \mathcal{D}_y^0 B_y^*$. Note that the multigrid Poisson solver uses the finite-difference operator $\mathcal{D}^+ \mathcal{D}^-$, not $\mathcal{D}^0 \mathcal{D}^0$, for the Laplacian ∇^2 . The resulting solution is not exact, but instead second-order accurate [1]. Exact, FFT-based Poisson solvers are another option, but limit the choices for boundary conditions. Furthermore, when using a centered-difference approximation to the divergence, exact Poisson solvers in general suffer from growth in checkerboard modes [19] in the field that, though divergence-free, are unphysical.

The Poisson solve yields the scalar field ϕ satisfying equation 18. We difference ϕ as follows to give the corrected field:

$$B_x^{n+1} = B_x^{*,n+1} - \mathcal{D}_x^0 \phi_{i,j} \quad (31)$$

$$B_y^{n+1} = B_y^{*,n+1} - \mathcal{D}_y^0 \phi_{i,j} \quad (32)$$

We find in our tests that an approximate projection does not have a significant impact on the quality of our results. Given its computational expense, we cannot recommend its use.

3.4 Riemann Solver

We solve the Riemann problem for ideal MHD using a linearized solver [28]. It employs characteristic analysis, like that of the normal predictor of Section 3.1, to solve for the state at cell edges. The eigenvalues and eigenvectors required for the characteristic analysis are sensitive to the input state; see Roe and Balsara [22]. Additionally, eigenvalue (ie. wavespeed) degeneracies can cause problems when the flow speed is close to zero. Errors due to degeneracies in the wavespeeds can build up in this case, causing numerical instability. We add a simple degeneracy fix to address this problem. (A similar problem occurs in the normal predictor, where problems can arise in the upwinding procedure used to preserve monotonicity. The same fix is used to address the problem there, as well.) Eigenvalues are modified when they are the same to within a chosen tolerance. So if the Alfvén speed $c_{A,x}$ is less than ϵ_P times the fast speed c_F , then we make the Alfvén and slow characteristic speeds, $\lambda_{\pm A}$ and $\lambda_{\pm S}$, equal to the advective speed λ_0 : $\lambda_{+A} = \lambda_{-A} = \lambda_{+S} = \lambda_{-S} = \lambda_0$. Similarly, if the slow speed c_S is less than ϵ_P times c_F , then we take the slow characteristic speeds equal to the advective one: $\lambda_{+S} = \lambda_{-S} = \lambda_0$. This modification occurs only when $\lambda_0 < 10^{-6} c_F$.

Based on experiments with degenerate and nearly-degenerate input states, we choose $\epsilon_P = 0.01$ so that the errors introduced are minimized while still preventing spurious wave strengths. The first condition handles degeneracy between the Alfvén and advective waves. This occurs when the field in the direction of interpolation is small. In this case the Alfvén and slow characteristic speeds are set to the advective speed. The second condition handles degeneracy between the slow and advective wave, and in that case only the slow characteristic speed is set to the advective speed.

For strongly nonlinear problems, it sometimes happens that the CFL condition is not sufficient to keep a scheme stable. If accelerations are large, velocities can grow such that in one timestep the pressure or density becomes negative. In order to dynamically adjust to such situations, we implement a scheme that checks for negative pressures or densities in either the predictor, Riemann solve, or corrector steps. If one is encountered, that timestep is restarted with the CFL number lowered by a factor of two, down to a minimum of one-eighth of the initial CFL number. Once the code has proceeded for several timesteps without again encountering negative values, the CFL number is raised by a factor of two, eventually reaching its initial value. Note that no matter the size of CFL number, the timestep is never allowed to increase by more than 10% in one iteration.

4 Numerical Tests

In this section, we compare the behavior of the code on a variety of linear and nonlinear problems. Both ideal and divergence-wave MHD codes were used. The code implementing the divergence-wave MHD algorithm also uses a predictor-corrector formalism. The characteristic analysis performed in the predictor steps uses an eighth wave carrying changes in the normal field, in addition to the seven waves of ideal MHD. As a result, in equation 10 of Section 3.1, the $(2, 2)$ entry of \mathbf{A} is equal to the advective speed u and not zero. The terms originally in a_B for ideal MHD cancel out, so that $a_B = 0$. Furthermore, this algorithm adds an extra source term,

$$S = - \left[0, \frac{B_x}{4\pi}, \frac{B_y}{4\pi}, \frac{B_z}{4\pi}, u, v, w, \frac{\vec{u} \cdot \vec{B}}{4\pi} \right]^T (\nabla \cdot \vec{B}), \quad (33)$$

to the right-hand side of the MHD equations 1-4. The source term is added in the transverse predictor and corrector steps. We note, however, that performing a MAC projection guarantees that $\nabla \cdot \vec{B} = 0$, and therefore the scheme is conservative and satisfies the jump relations. (Contrast this with the situation described in T00, where a non-conservative divergence wave scheme produced

shock tube results which did not satisfy the jump conditions.) This is done in all runs with the divergence-wave scheme.

For both MHD implementations, different variations on the base algorithm were tested. Due to problems evident in the divergence-wave results, we restrict our presentation largely to the ideal MHD results.

In what follows, codes with conservative filtering are labeled with a 'C', and those with non-conservative filtering an 'N'. A 'P' denotes codes with an approximate projection. So, for example, a conservatively filtered code with approximate projection is labeled 'CP'.

4.1 Simple Linearized MHD Waves

We tested the performance of the code on all four varieties (advective, fast, slow, and Alfvén) of linearized MHD waves. These tests comprised waves propagating along x- and y-axes (wavenumbers $\vec{n} = (1, 0)$ and $\vec{n} = (0, 1)$), along with waves at slopes of 1:1 ($\vec{n} = (1, 1)$) and 2:1 ($\vec{n} = (2, 1)$). The simulation domain had length $L = 1$ in both dimensions, and the boundaries in all cases were periodic. The Alfvén waves used $\rho_0 = 1$, $\vec{u}_0 = 0$, $\vec{B}_0 = B_0 \hat{b} = \sqrt{4\pi} \hat{b}$ with unit vector $\hat{b} = (\frac{1}{\sqrt{2}}, \frac{1}{\sqrt{2}})$, and $P_0 = 1$. The perturbation δW is

$$\delta W = \begin{bmatrix} 0 \\ 0 \\ 0 \\ -c_A \\ 0 \\ 0 \\ B_0 \\ 0 \end{bmatrix} \delta_{\text{pert}} \sin(\vec{k} \cdot \vec{x}), \quad \text{with } \vec{k} = 2\pi\vec{n}, \quad (34)$$

where \vec{n} is the aforementioned vector of integers chosen so as to be consistent with the periodic boundaries. The Alfvén speed $c_A = B_0/\sqrt{4\pi\rho_0} = 1$.

Fast and slow wave expressions are somewhat more complicated. In this case, \hat{b} lies at 45 degrees from the unit wavevector \hat{k} , all other aspects of the unperturbed state remaining unchanged from the Alfvén case. The perturbation is

$$\delta W = \begin{bmatrix} \rho_0 \\ \frac{\sqrt{2}c_{F/S}^2\hat{b}_y - a^2\hat{n}_y}{c_{F/S}} \\ \frac{a^2\hat{n}_x - \sqrt{2}c_{F/S}^2\hat{b}_x}{c_{F/S}} \\ 0 \\ -\sqrt{2}B_0\frac{c_{F/S}^2 - a^2}{c_A^2}\hat{n}_y \\ \sqrt{2}B_0\frac{c_{F/S}^2 - a^2}{c_A^2}\hat{n}_x \\ \rho_0 a^2 \end{bmatrix} \delta_{\text{pert}} \sin(\vec{k} \cdot \vec{x}) \quad (35)$$

$$a^2 = \frac{\gamma P_0}{\rho_0} \quad (36)$$

$$c_{F/S}^2 = \frac{1}{2} \left(a^2 + c_A^2 \pm \sqrt{c_A^4 + a^4} \right) \quad \text{corresponding to fast/slow speeds} \quad (37)$$

$$\hat{n} = (\hat{n}_x, \hat{n}_y) = \frac{\vec{n}}{|\vec{n}|} \quad (38)$$

All tests gave results consistent with second order accuracy, although waves at 2:1 showed slightly smaller (≥ 1.8 , versus 2.0) rates of convergence in some components. The modifications suggested by Stone were essential in obtaining second-order convergence for the 1:1 and 2:1 slope tests, increasing the convergence rates from first- to second-order for waves propagating along the diagonal. An example of the convergence rates for small amplitude fast waves is given in Table 1.

Component	Pre-Correction	Post-Correction
ρ	0.977	2.03
v_x	1.40	2.03
v_y	1.15	2.02
B_x	1.60	2.01
B_y	1.57	2.02
P	0.977	2.03

Table 1

Convergence rates by component for fast waves ($\delta_{\text{pert}} = 10^{-5}$) propagating at 45 degrees, for ideal MHD code before and after corrections suggested by Stone. [27]

A more stringent test of the code is to advect the linearized waves so that their profile remains stationary. In these tests, the background state has a non-zero velocity equal to the wavespeed:

$$\text{Alfvén: } \vec{u}_0 = -c_A \hat{n} \quad (39)$$

$$\text{Fast/Slow: } \vec{u}_0 = -c_{F/S} \hat{n} \quad (40)$$

An analysis of the eigenstructure of MHD shows (Appendix A) that such waves should cause trouble for the ideal MHD codes that do not suppress non-solenoidal fields. Errors generated in this case are not advected away, causing difficulty in the case that they are not diffused or otherwise dealt with. We find that the ideal MHD code without a MAC projection goes unstable for low amplitude ($\delta_{\text{pert}} = 10^{-4}$) fast waves with \hat{n} at 2:1 slope. The instability starts as a high frequency oscillation in the field parallel to \vec{n} . It grows with time and spreads to the other components, causing a low order of convergence even at early times. Once the oscillations reach a certain level, they drive the code unstable. The oscillations are almost completely absent, and the code stable, in our ideal MHD codes using a MAC projection. Adding filtering of the field further reduces the errors. A code including filtering but no MAC projection is also stable to deficient waves. We conclude that either a MAC projection or filtering is essential to stability for this class of problems; in all subsequent runs the base ideal MHD code will include a MAC projection. (Filtering is less costly computationally, but we later find the MAC projection to be essential for certain non-linear problems.) When used in conjunction with a MAC projection, filtering results in a somewhat higher rate of convergence than unfiltered codes, so that the filter add an extra measure of accuracy in this case.

4.2 Decay of Linearized MHD Waves

The equations of ideal MHD neglect the effects of viscosity and electrical resistivity. Numerical dissipation, however, can affect the solution in ways that mirror these physical effects. Following Ryu, Jones, and Frank [23] (hereafter RJF95), we measure the decay of Alfvén, fast, and slow waves, and use the implied physical resistivity as a measure of the numerical resistivity of our ideal MHD scheme.

We use exactly the same set-up as RJF95, with Alfvén, fast, and slow waves propagating at a 1:1 slope and wavelength of $\sqrt{2}$ times the length of one side of the computational domain. The decay of these waves was measured by fitting a decaying exponential to a measure of the wave strength,

$$\varepsilon = \sum_{i,j} l_k \cdot (\delta W)_{i,j}, \quad (41)$$

where $(\delta W)_{i,j} = W_{i,j} - W_0$ is the perturbation in the primitive variables. l_k is the left-eigenvector associated with the mode in question, evaluated at W_0 , the unperturbed state. Figure 2 shows the dependence of the decay rate on

resolution for runs with number of cells per dimension $N = 16, 32, 64, 128, 256$, and 512 . Comparison with Figure 4 of RJF95 reveals a much smaller decay rate for our unsplit method. Furthermore, we find that the decay rate varies according to the power law $\Gamma \propto N^{-3}$, not N^{-2} . The former is consistent with second-order accuracy, since the truncation errors have the following form:

$$\tau = C_2(\Delta x)^2 \frac{\partial^3 U}{\partial x^3} + C_3(\Delta x)^3 \frac{\partial^4 U}{\partial x^4} + \mathcal{O}(\Delta x^4). \quad (42)$$

We see here that the second-order error term is proportional to $\frac{\partial^3 U}{\partial x^3}$, which is dispersive in nature. The third-order term is the first error term that is dissipative. As a result, we expect the resistivity to decrease as Δx^3 , or N^{-3} . We posit that the smaller decay rates $L\Gamma/c$ and larger exponent describing

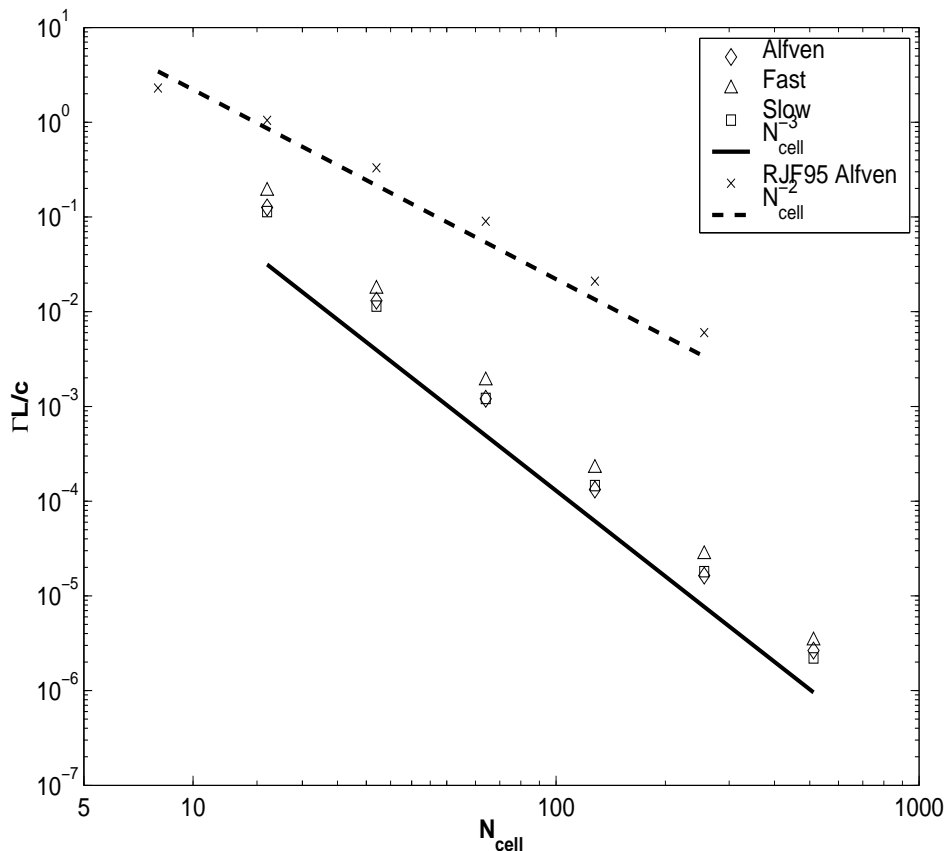


Fig. 2. Normalized damping rate versus resolution for the decay of Alfvén, fast, and slow modes propagating at a 1:1 slope. The calculations were done at resolutions of 16×16 , 32×32 , etc. up to 512×512 .

the rate of decrease of Γ with increasing resolution can be attributed to one or both of two effects. The first is the unsplit methodology used in the scheme presented here. The second is the multidimensional corrections described in Section 3.1, which played a pivotal role in obtaining second-order accuracy on linearized MHD waves much like those used in this test.

4.3 MHD Shock Tube

The second test is the MHD shock tube problem from Ryu, Jones, and Frank [23]. The solution consists of two fast shocks, one slow shock, one slow rarefaction, and a contact discontinuity. We have run the problem in two orientations: (1) with the shock velocity aligned with the x-axis of the computational domain (referred to below as 1-D), and (2) with this velocity inclined at a 2:1 slope. The latter configuration follows the 2-D shock tube test case from T00. It was chosen in order to test the multidimensional behavior of the code, meanwhile ensuring there were no serendipitous cancellations of errors, as might be the case in a 45° inclined case. In runs of a 1-D tube at R_{512} (ie. on a grid with 512 cells per linear dimension) and to a time of $t = 0.08$, we are able to reproduce the results given in Table VI of Dai & Woodward [10] (hereafter DW94) with errors of $\leq 0.12\%$. These results are independent of the type of filter used and whether an approximate projection was performed. When combined with an observed first-order convergence rate, they give us great confidence in the performance of our code on 1-D shock tube problems.

The inclined version of this shock tube problem was run on grids of size $2N \times N$, with $N = 64, 128$, and 256 . We compared these results with the 1-D shock tube results by first taking a cut of the data that included all cells lying along a line at 2:2 slope ($\alpha = 26.57^\circ$), starting from the first cell in the domain. Then, all velocities and fields in this cut were rotated by $-\alpha$. A check using the initial conditions showed that such a cut of the inclined initial conditions matched perfectly with the 1-D shock tube ICs outside of the jump region. (In the jump region, the inclined ICs were slightly different due to the volume averaging performed in producing them. This leads the initial jump to be spread over two zones instead of one.) Note that we chose the grid spacing for the 1-D runs to be a factor of $\sqrt{5}/2$ bigger than the incline grid spacing, so that the shock covers the same distance in physical space in a given time.

Figure 3 shows results for the inclined shock tube overlaid on the aligned result. They compare a R_{512} 1-D run with a $N = 256$ 2-D run that has equivalent effective grid spacing. The ideal MHD codes shown give fractional errors with an L^1 norm of less than 0.8% , averaged over all components. Note that the filtered code gives much smaller errors in the normal field (3% versus 16%) than the unfiltered version. As illustrated here and by Figure 11 in T00, shock-capturing codes generally produce a jump in the normal component of the magnetic field in non-grid-aligned shock tube problems such as this. More generally, such codes exhibit non-monotonic behavior inside the shock structure, so that Riemann invariants are not exactly preserved there [30]. We find that the observed jumps are indeed limited to the region of the shocks, and in our base ideal MHD code have a very similar magnitude to that shown in the T00 results. Most importantly, despite errors in B_n inside the jump

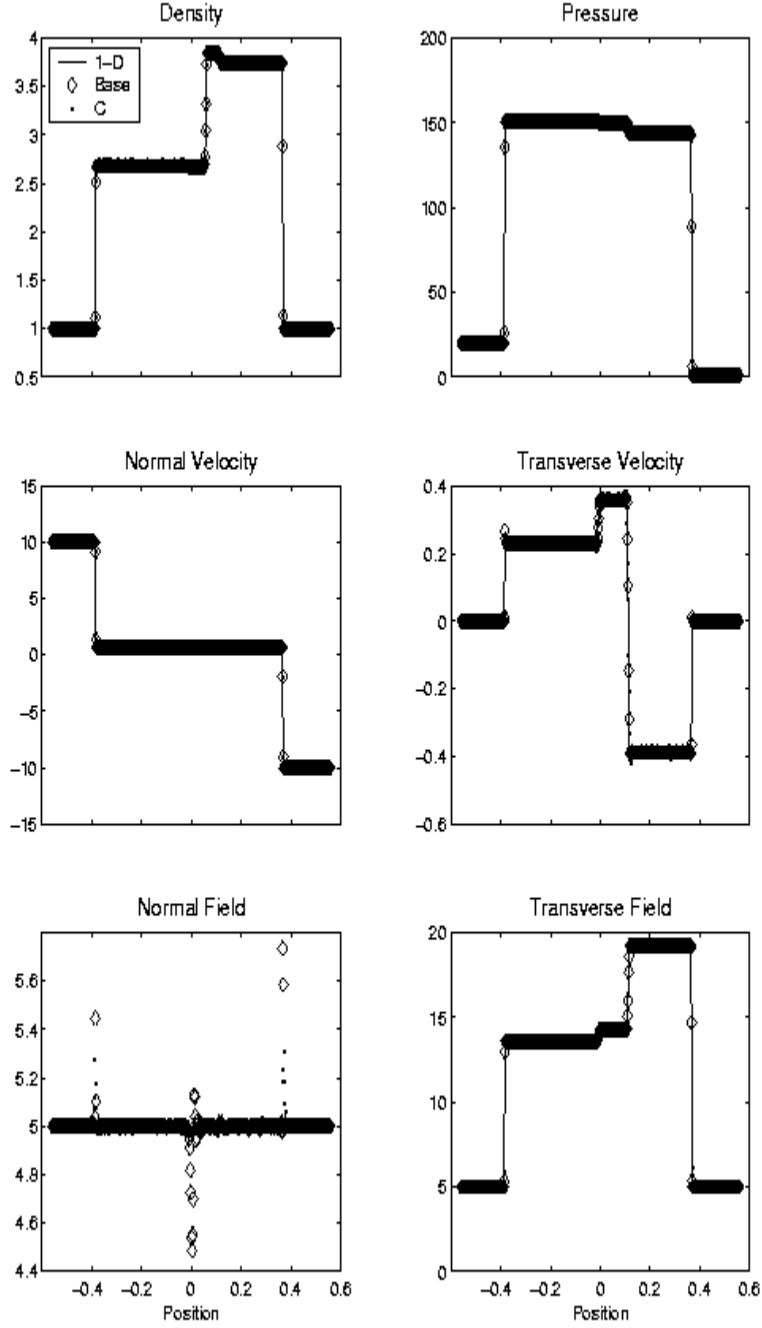


Fig. 3. MHD shock tube comparison by component. The 1-D shock tube (line) is used as a basis for comparison with 2-D shock tube runs with same effective resolution. The jumps in normal field B_n are expected, and the size of the jumps for the Base code is similar to that published in Tóth 2000.

region, the jump relations are still satisfied outside of it.

Figures 4 and 5 show plots of error versus resolution for the 2-D shock tube runs. We see that the decrease in the error in B_n afforded by use of an approximate projection does not bring a corresponding decrease in errors in the normal velocity (or any other component). This being the component we expect on physical grounds to be most affected by spurious jumps in the normal field, we conclude that the projection is not necessary to give physically correct results in shock tube problems.

While the conservative filter does improve the errors in the normal field drastically, Figure 3 shows that it produces more oscillatory behavior near the inclined shock fronts, particularly in the transverse velocity. This behavior shows up in the error versus resolution plots in Figure 4 as well, where we see larger errors than the base code in the transverse velocity (and transverse field). The convergence rates remain first-order nonetheless. We infer that a tradeoff exists between reduction of the normal field errors and the production of oscillatory effects in the transverse direction when using such a filter. A smaller value of the filtering coefficient is expected to produce less oscillatory behavior and more of an error in B_n .

Figure 4 shows that the errors in the ideal MHD case fall off most quickly for the base algorithm (label 'Base') and the conservatively filtered codes (labels 'C' and 'CP'); the component-averaged slopes are ≤ -0.97 , implying first-order convergence. The non-conservatively filtered codes (labels 'N' and 'NP' of Figure 4) and divergence-wave MHD codes (Figure 5) do not converge at first-order for this problem, implying that their accuracy on problems with strong, non-grid-aligned shocks is suspect.

We make note of several further features in these graphs. First, there is a notably larger error in v_t and B_t , similar to that noted above for the conservatively filtered code, in the ideal MHD code without a MAC projection (label 'no MAC' in Figure 4). This is somewhat surprising, since we expect B_n to be the component most affected by the presence of divergence cleaning. Second, both the non-conservatively filtered ideal MHD codes (labels 'N' and 'NP') and, even more conspicuously, the divergence-wave MHD codes evidence a fall-off of the convergence rate with increasing resolution. This is most evident in the pressure and density components. For the ideal MHD codes, this effect is attributable to the loss of energy conservation associated with this filter. In the divergence-wave MHD codes, it can be attributable to the effects of the divergence wave itself, since the fall-off occurs in the base code (label 'Base' in Figure 5) as well.

Table 2 gives the fractional errors, again relative to a high resolution 1-D shock tube run, in each component and averaged over all components. They are not much different in magnitude than those given in T00, Table III. Taken together, Table 2 and Figure 4 illustrate that where the fractional error is not a good discriminator between codes, the convergence rates of these codes can be a very good guide.

Code	$\delta\rho$	δp	δv_n	δv_t	δB_n	δB_t	$\bar{\delta}$
Base	0.00290	0.00170	0.00492	0.0167	0.00404	0.00257	0.00458
N	0.00502	0.00401	0.00357	0.0311	0.00378	0.00584	0.00747
NP	0.00524	0.00427	0.00398	0.0319	0.000992	0.00637	0.00750
C	0.00299	0.00180	0.00495	0.0292	0.00346	0.00433	0.00639
CP	0.00302	0.00182	0.00506	0.0299	0.000850	0.00458	0.00622

Table 2

Relative error, by component and averaged, for the 2-D MHD shock tube problem. Results are given for codes solving the ideal MHD equations. The base code includes only a MAC projection, while the others add conservative (C) or non-conservative (N) filters and possibly an approximate projection (P). The errors were calculated using the same procedure as in Tóth (2000), Table III.

We rule out further use of the divergence-wave code at this point due to the aforementioned problems on the incline shock tube problem, plus the fact that the divergence-wave code was unstable to degenerate Alfvén and fast stationary waves even with the MAC projection. We were somewhat surprised to find lower than first-order convergence on the incline shock tube problem. This can be attributed to the two differences between the ideal MHD and divergence-wave MHD algorithms. The first is the divergence wave added to the eigenstructure, which causes jumps in B_n to be advected with the flow. The second is the effect of the added source terms (equation 33) on the transverse predictor, where they enter into the calculation of the fluxes in equation 9.

4.4 Magnetized Flux Tube

This problem involves a high-field, low gas pressure region bounded on both sides by a high-gas pressure, zero-field region. The base state has the entire 2-D domain in pressure balance. The boundaries between magnetized and unmagnetized regions are discontinuous and lie along $x = \pm 0.2$. In both regions, $\rho = 1$, $\vec{u} = 0$ and $B_x = B_z = 0$ initially. In the magnetized region, $x \in [-0.2, 0.2]$, $B_y = \sqrt{80\pi}$ and $P = 1$. Outside of this, $B_y = 0$ and $P = 11$. To the background state is added a sinusoidal perturbation upon the x-velocity

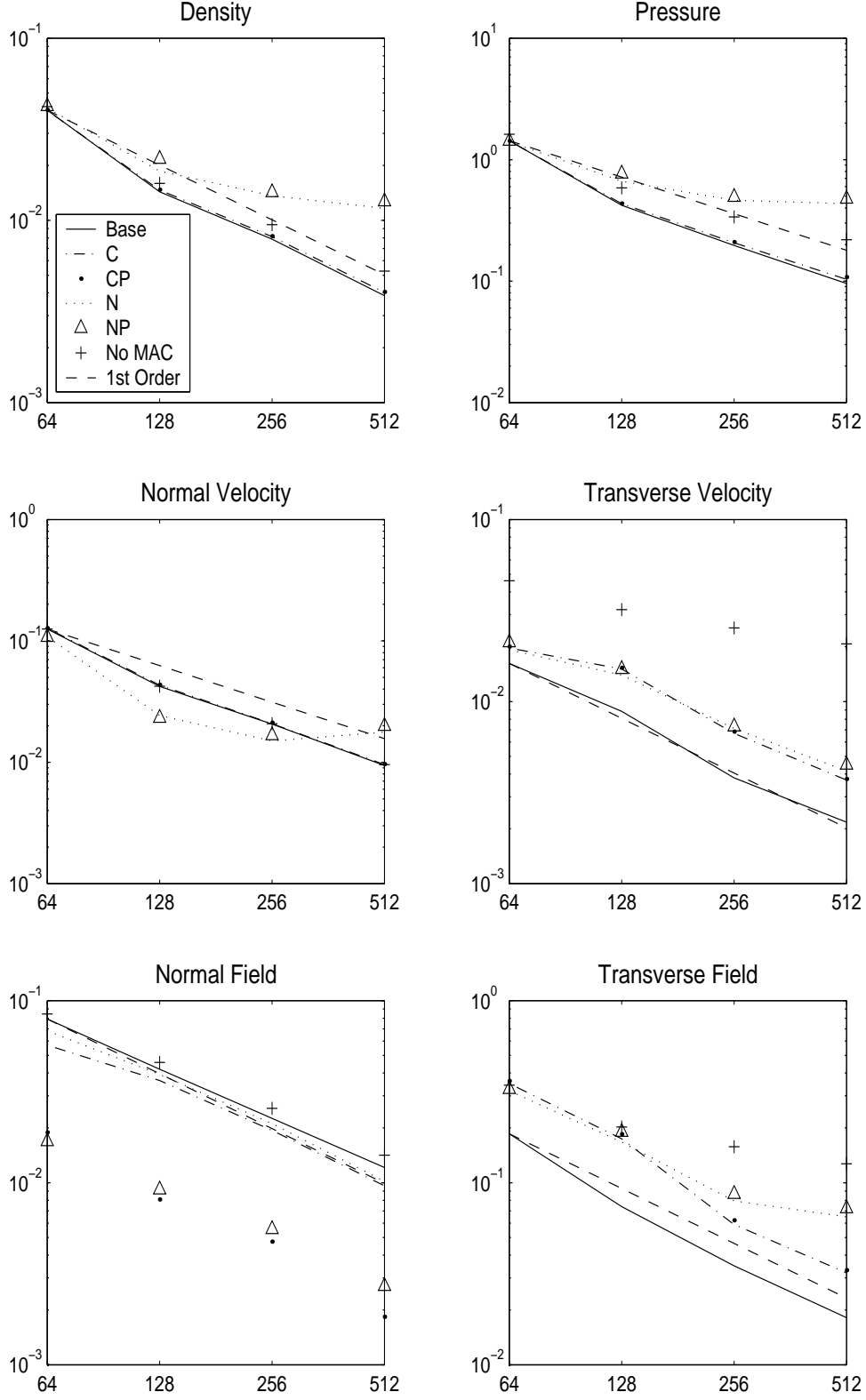


Fig. 4. L^1 norm of error versus resolution (number of cells per dimension) for 2-D MHD shock tube run with codes solving the ideal MHD equations. The dashed line is a fiducial showing first-order fall-off of errors. The line labeled 'no MAC' has no divergence-cleaning of the edge-centered states.

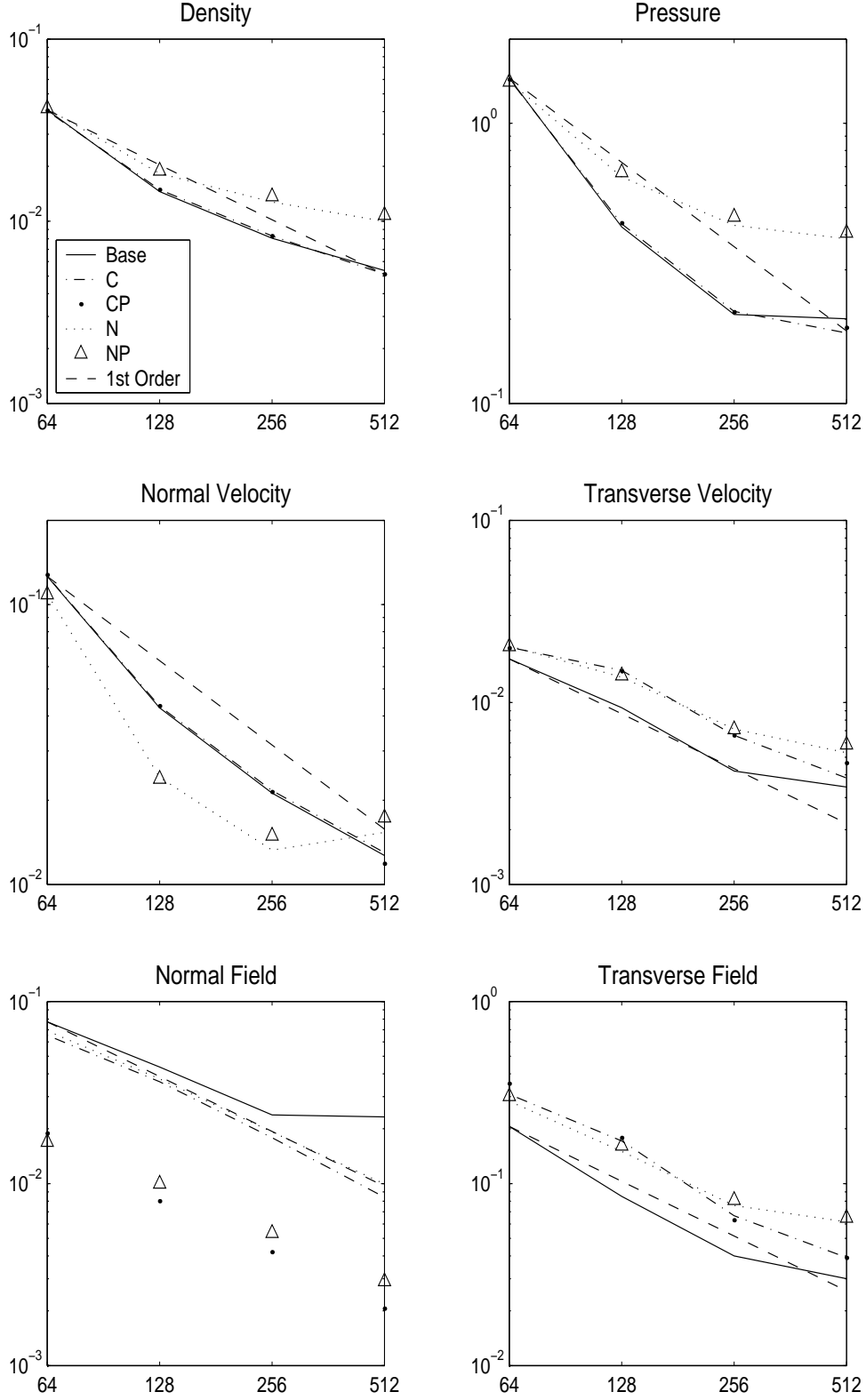


Fig. 5. L^1 norm of error versus resolution (number of cells per dimension) for 2-D MHD shock tube run with codes solving the divergence-wave MHD equations. The dashed line is a fiducial showing first-order fall-off of errors.

whose amplitude is $\delta_{\text{pert}} = 0.01$ times the Alfvén speed, and covers the entire domain:

$$\delta u = \delta_{\text{pert}} c_A \sin(2\pi y) \quad \text{and} \quad \delta \vec{B} = \delta \rho = \delta P = \delta v = \delta w = 0 \quad (43)$$

The Alfvén speed in this case is $c_A = B_0/\sqrt{4\pi\rho} = \sqrt{20}$. The strong discontinuity in the field is expected to cause problems for algorithms that do not suppress non-solenoidal fields. In particular, at the stagnation points where the perturbation velocity is zero, truncation errors leading to non-solenoidal fields can build up and cause numerical schemes to go unstable. This is in fact what we find for the ideal MHD scheme run without a MAC projection. Non-solenoidal fields build up at these stagnation points, causing the production of spurious velocities and triggering numerical instabilities.

Figure 6 shows the initial conditions for the flux tube problem. The perturbation plucks the field. After an initial transient at start-up, the perturbation develops into a standing wave in the magnetized region. The unmagnetized region sloshes back and forth from one side of the flux tube to the other, owing to the periodic boundary conditions. Because of the slightly different frequencies of these two oscillations, we expect the initial velocity perturbation to cause standing Alfvénic waves in the magnetized region, and compressive waves at the boundaries of the tube. The change in the internal energy tracks the compressive waves. The problem was run to a time $t = 6.0$, corresponding to about 60 Alfvén crossings of the short dimension of the tube. This was enough time for the problem to reach a steady state and subsequently evolve for many periods of the oscillations.

All versions of our code performed almost identically on this test, as evidenced by Figure 7. One difference lies in a small decrease in the total energy for the schemes employing the non-conservative filter. This decrease, less than 0.01% for the R_{512} runs shown, is not serious. Also, the cell-centered divergence of the field is smaller for filtered codes than the base code. It is even smaller when the approximate projection is employed. We note, however, that the decrease in this measure of the monopoles afforded by use of filters does not seem to have affected the dynamics of the tube.

4.5 *Inclined Flux Tube*

A second version of the flux tube problem, in which it is inclined at an angle of 45 degrees with respect to the original, is better at differentiating between the algorithms. In this case, the boundaries between magnetized and unmagnetized regions are four in number (the tube must wrap through the physical domain twice, owing to the periodic boundary conditions), lying along

$x + y = -0.8$, $x + y = -0.5$, $x + y = 0.2$, and $x + y = 0.5$. In both regions, we have $\rho = 1$, $\vec{u} = 0$ and $B_z = 0$ initially. In the magnetized region, $B_x = -\sqrt{40\pi}$, $B_y = \sqrt{40\pi}$, and $P = 1$. In the unmagnetized region, $P = 11$ and $B_x = B_y = 0$. The perturbation is again applied to the entire domain, and has strength $\delta_{\text{pert}} = 0.01$:

$$\delta u = \delta_{\text{pert}} \frac{c_A}{\sqrt{2}} \sin \left(2\pi \frac{-x + y}{\sqrt{2}} \right) \quad (44)$$

$$\delta v = \delta_{\text{pert}} \frac{c_A}{\sqrt{2}} \sin \left(2\pi \frac{-x + y}{\sqrt{2}} \right) \quad (45)$$

$$\delta \vec{B} = \delta \rho = \delta P = \delta w = 0 \quad (46)$$

One effect of rotating the flux tube is the addition of a numerical perturbation, or gridding effect. The volume-averaging required for producing the initial conditions creates a region of intermediate pressure and field between the fully magnetized and unmagnetized regions. This transition region becomes smaller as the resolution is increased. Other differences are the width of the tube, which was thinner for the inclined case since it had to cross the periodic domain twice. Therefore, we expect the start-up dynamics and period of oscillation to be somewhat different in the incline case. We do expect, however, many qualitative similarities between the two sets of results.

Figure 8 shows a resolution study of the incline flux tube, with global quantities plotted out to $t = 5$. (This is about 50 Alfvén crossing times; a shorter time was chosen in order to show more detail. All codes which were stable to this time were also stable out to $t = 6$.) Notice that the MAC projection keeps the L^1 norm of the monopole component in the edge-centered field below 10^{-12} , and the filter damps the monopole component of the cell-centered field. In fact, several possibilities exist for measuring the divergence of the cell-centered field. Besides a centered difference, to which checkerboard modes are transparent, there are two discretizations consistent with the filter equations, 28 and 29:

$$\nabla^{\text{Filter}} \cdot \vec{B} := \mathcal{D}_x^0(B_x)_{i,j} + \frac{1}{2}(\mathcal{D}_y^0(B_y)_{i+1,j} + \mathcal{D}_y^0(B_y)_{i-1,j}) \quad (47)$$

$$\nabla \cdot \vec{B} := \frac{1}{2}(\mathcal{D}_x^0(B_x)_{i,j+1} + \mathcal{D}_x^0(B_x)_{i,j-1}) + \mathcal{D}_y^0(B_y)_{i,j}. \quad (48)$$

They both catch checkerboard modes in the field; we choose the first of these two in tracking the divergence.

The solutions to the incline flux tube in Figure 8 are converged in the L^1 norm of the transverse velocity v_t , and nearly so for the normal velocity v_n . The kinetic energy graph has a hump in the R_{64} run which is absent in the higher resolution runs. This phenomenon shows up in other runs as well; see Figure 9.

For smaller filtering coefficients, the magnitude of the hump decreases. However, for the base code (equivalent to a filtering coefficient of zero), the code was unstable. We infer a trade-off between stability (high filtering coefficient C) and accuracy (low C). For this plot we chose a filtering coefficient which gave stability at all resolutions run, while keeping the size of the hump as small as possible.

The expected qualitative similarities between aligned and incline flux tube results are present, such as oscillations in kinetic and magnetic energy of similar magnitudes. The size of the oscillations in the L^1 norm of v_t and v_n are also similar. There are also substantial differences. In figure 9, notice that the base code goes unstable on this problem (the results stop before the end time of $t = 6 \simeq 60t_{\text{Alfven}}$). Negative pressures and densities appear in the solution that, through repeated occurrences, drive the scheme unstable.

Another difference between the incline and 1-D tubes lies in the timing of the aforementioned hump in the L^1 norm of the transverse and normal velocities. For the incline tube, the rise begins after about $t = 1$, while for the 1-D tube it begins almost immediately. The magnitudes of the two jumps are similar. The kinetic energy reflects this: for the codes employing the $C = 0.125$ filter, it rises early on to about twice the value in the base code, later settling to a somewhat larger steady state value. The magnitude of this increase is directly tied to the filtering; when a smaller filtering coefficient $C = 0.0078125$ is used, it goes down. It is not, however, dependent on the type of filter used; compare lines labeled 'N 0.0078125' and 'C 0.0078125'. This leads one to surmise that it is the magnetic effects of the filter, and not any internal energy effects, that are causing this kinetic energy increase.

The internal energy of non-conservative schemes differs considerably from that of the base and conservative filter schemes. The internal energy of the non-conservative schemes is lower (for a given resolution) than for the conservatively filtered schemes, or even the aligned flux tube. The smaller internal energy is reflected in the total energy, leading us to surmise that this energy is lost, and not a reflection of less numerical resistivity. Furthermore we note that the base scheme, whose lack of a filter means that it does not convert magnetic energy into internal energy, shows an internal energy profile similar to that of the conservatively filtered scheme. This lends further weight to the hypothesis that it is the non-conservative code whose internal energy is too low, not the conservatively filtered code whose is too high.

5 Conclusions

We have presented an unsplit method for ideal MHD which shows no effects of non-solenoidal fields, while retaining the co-location of all physical quantities at cell-centers. The latter point is important because such a uniform centering makes it easier to extend the scheme to adaptive meshes, and has the advantage of using a well-understood Godunov method for time integration. These are in contrast to the Constrained Transport (CT) approach, where staggered grids add additional software complexity. Furthermore, it is not obvious how to discretize diffusion operators to include non-ideal MHD effects on staggered grids. Lastly, we add that the effective advection scheme for the magnetic field components is not of the standard type, and it is unclear what its properties are in the presence of underresolved gradients.

The MAC projection of fields at cell-edges and filtering of the cell-centered fields are found to be essential to stability and accuracy. The computational cost of projection is not insignificant, and adds additional software complexity. We note, however, that recent work with Poisson solvers on adaptive grids ([3,18]) have made this computational cost smaller than that of the hyperbolic update.

Use of a filter alone on linear problems reduces computational cost and does not affect accuracy. We find that both filter and MAC projection are required on strongly nonlinear problems such as the incline flux tube, albeit with a lowered value of the filter coefficient in order to preserve accuracy. Also essential to the accuracy of the scheme are the modifications suggested by Stone – linear waves not propagating along cardinal directions are not second-order accurate without it. The approximate projection, on the other hand, had very little effect on either the order of accuracy or stability of the schemes, a fact that, coupled with its computational cost, makes it less than desirable.

We found that in determining the accuracy of our code, measuring the rate of convergence on nonlinear problems was a superior metric to comparison of errors at a single resolution. Significant differences were found between the convergence rates even of individual primitive variables. These data can be crucial in choosing between different algorithmic variants of a base code. As a result of convergence test results, we were able to rule out use of divergence-wave codes and also the non-conservative filter due to poor performance on the shock tube problem. We encourage future authors to incorporate convergence testing of simple nonlinear problems such as the shock tubes run here into their test suites.

Overall the ideal MHD code with MAC projection and a conservative filter performed best on the suite of tests presented. Filtering of the magnetic field

was important to code stability in the nonlinear problems, and accuracy in the deficient wave problems. A filtering coefficient as high as $C = 0.125$ left the code second-order on linear problems. This should be regarded as a maximum, however, and a lower value was required in the strongly non-linear flux tube problem. By experimenting with the filtering coefficient, we were able to find a value for which this problem remained stable without adversely affecting the accuracy of the underlying scheme.

The magnetized, perturbed flux tube constitutes a strong test of the stability of our schemes. The combination of a stationary discontinuity, low ratio of thermal to magnetic pressure (beta), and imposed perturbation caused significant problems for the unsplit code without projection or filter. With a suitably chosen value of the filtering coefficient, the conservative filter helped stability and worked to decrease the magnitude of a centered-difference measure of the divergence of the field.

6 Acknowledgements

The authors would like to thank Jim Stone for pointing out the missing multidimensional MHD terms.

The research of Robert K. Crockett was supported in part by A Division at Lawrence Livermore National Laboratory.

The research of Christopher F. McKee was supported in part by NSF grant AST-0098365.

Work at the Lawrence Berkeley National Laboratory is sponsored by the US Department of Energy Applied Mathematical Sciences program under contract DE-AC03-76SF00098 and by the NASA Earth and Space Sciences Computational Technologies Program under interagency agreement number S-44830-X.

The research of Richard I. Klein was supported in part by a NASA ATP grant NAG5-12042. Both Richard I. Klein and Robert T. Fisher are supported under the auspices of the US Department of Energy at the *Lawrence Livermore National Laboratory under contract W-7405-ENG-48.

A Appendix A: Divergence Constraints, Modified Equation Analysis, and Eigenvector Deficiencies

In this section, we will present a heuristic analysis of the effect of numerical errors in the divergence-free constraint on the stability of finite-difference methods for the ideal MHD equations. Our starting point will be the modified equation approach to analyzing the effect of truncation error on solution error. For any finite difference method, the modified equation is given by the original system of PDEs, with forcing terms given by the truncation error. In the present setting, the modified equation takes the following form:

$$\partial_t U^{Mod} + \nabla \cdot \vec{F}(U^{Mod}) = \tau_U(U^{Mod}) \quad (\text{A.1})$$

$$\nabla \cdot U^{Mod} = \tau_D(U^{Mod}). \quad (\text{A.2})$$

Here τ_U is the usual truncation error for the numerical method obtained from applying the difference operator to a solution to the differential equation evaluated on the grid. The equation for the evolution of τ_D is obtained by taking the divergence of the modified equation for the evolution of U^{Mod} ,

$$\partial_t \tau_D = \nabla \cdot \tau_U. \quad (\text{A.3})$$

The truncation error forcing terms mimic the effect of numerical error on the computed solution. Specifically, we expect U^{Mod} , the solution to the modified equation, to satisfy $\|U^{\Delta x} - U^{Mod}\| = \mathcal{O}(\Delta x^{p+1})$, where $U^{\Delta x}$, the solution obtained from the p^{th} -order scheme on a grid with spacing Δx , satisfies $\|U^{\Delta x} - U\| = \mathcal{O}(\Delta x^p)$.

In particular, for MHD, the effect of numerical error can be understood in terms of the truncation-error forcing in the modified equation causing the solution to violate the divergence-free constraint. Without that constraint being satisfied, the remaining ideal MHD equations can exhibit eigenvector deficiencies in the linearized-coefficient matrix \mathbf{A} , leading to anomalous loss of regularity and ill-posedness. In the numerical simulation, this translates into loss of accuracy and possibly instability of the underlying difference method.

To see this, we consider the case of a small-amplitude wave corresponding to one of the eigenmodes of \mathbf{A} (see Equation 11):

$$W(\vec{x}, t) = W_0 + \alpha(x - \lambda_k t)r_k \quad (\text{A.4})$$

$$\mathbf{A}_0 r_k = \lambda_k r_k \quad r_k = (\tilde{r}_k, 0)^T. \quad (\text{A.5})$$

Then $W(\vec{x}, t)$ satisfies the MHD equations up to terms of $\mathcal{O}(\alpha^2)$.

Without loss of generality, we take the direction of propagation to be in the x-direction in 3-D. However, we allow our computational spatial grid to have an arbitrary orientation in space. In that case, the modified equation corresponding to our numerical solution to the PDE in primitive variables W is given by (see Equation 10)

$$\partial_t W^{Mod} + \mathbf{A}_0 \partial_x W^{Mod} = \tau_W \quad (\text{A.6})$$

$$W^{Mod} = (\tilde{W}^{Mod}, B_x^{Mod}). \quad (\text{A.7})$$

The modified equation dynamics can be reduced to the following system of two equations:

$$\alpha^{Mod} = l_k \cdot (\tilde{W}^{Mod} - \tilde{W}_0) \quad (\text{A.8})$$

$$\partial_t \alpha^{Mod} + \lambda_k \partial_x \alpha^{Mod} + (l_k \cdot a_B) \partial_x B_x^{Mod} = l_k \cdot \tilde{\tau} \quad (\text{A.9})$$

$$\partial_t B_x^{Mod} = \tau_B \quad (\text{A.10})$$

In the system here, if one of the computational spatial grid coordinate axes is aligned with \hat{x} , $\tau_B \equiv 0$. However, if the direction of propagation is not aligned with one of the computational coordinates, then in general $\tau_B \neq 0$. If $l_k \cdot a_B \neq 0$ and $\lambda = 0$, then the left-hand side of A.8-A.10 is an example of a first-order system with an eigenvector deficiency. Such systems have an obvious loss of spatial regularity: α^{Mod} grows like the derivative of τ_B . This is in contrast to the behavior of well-posed hyperbolic systems, in which the solution has the same spatial regularity as the forcing. In other words, since regularity implies that there are as many derivatives in the solution as in the forcing term, discontinuous forcing of a hyperbolic system leaves the problem ill-posed. Discontinuity in τ_B implies that α^{Mod} can grow without bound, owing to its dependence on the derivative of τ_B .

In terms of a numerical method, we expect that the presence of such terms would lead to either an anomalous loss of accuracy or numerical instability. In the latter case, the forcing of α^{Mod} in A.9 takes the form of a finite difference operator applied to B_x^{Mod} , whose spatial variation is due entirely to τ_B . If τ_B fails to be smooth, either because of lack of smoothness in the initial data or in the finite difference formulae (eg. limiters), such lack of smoothness is immediately amplified.

This discussion also provides an explanation for the behavior of the method described here. The use of the MAC projection and the filter does not eliminate the truncation error terms that lead to the eigenvector deficiency, but regularizes it by smoothing. For example, the application of the filter in the plane-wave example corresponded to adding a diffusion term to the equation

for B_x^{Mod} ,

$$\partial_t B_x^{Mod} = \tau_B + \eta \partial_x^2 B_x^{Mod}, \quad (\text{A.11})$$

with $\eta = \mathcal{O}(\Delta x)$. The use of the filter alone is sufficient to stabilize the small-amplitude plane wave solution in Section 4.1, and in that case leads to a second-order accurate result. The MAC projection performs a more drastic smoothing, but only on the intermediate form of B_x^{Mod} used to compute $\partial_x B_x^{Mod}$ in equation A.9.

References

- [1] A. S. Almgren, J. B. Bell, and W. Szymczak, A numerical Method for the Incompressible Navier-Stokes Equations Based on an Approximate Projection, *SIAM J. Sci. Comput.* **17** (1996) 358.
- [2] D. S. Balsara, Total Variation Diminishing Scheme for Adiabatic and Isothermal Magnetohydrodynamics, *Astrophys. J. Suppl.* **116** (1998) 119.
- [3] G. Balls and P. Colella, A Finite Difference Domain Decomposition Method Using Local Corrections for the Solution of Poisson's Equation, *J. Comput. Phys.* 180 (2002) 25-53.
- [4] D. S. Balsara and D.S. Spicer, A Staggered Mesh Algorithm Using High Order Godunov Fluxes to Ensure Solenoidal Magnetic Fields in Magnetohydrodynamic Simulations, *J. Comput. Phys.* **149** (1999) 270.
- [5] J. B. Bell, P. Colella, and L. H. Howell, An Efficient Second-Order Projection Method for Viscous Incompressible Flow, in *AIAA 10th Computational Fluid Dynamics Conference Proceedings*, June 1991, 360.
- [6] J. B. Bell, P. Colella, and J. A. Trangenstein, Higher Order Godunov Methods for General Systems of Conservation Laws, *J. Comput. Phys.* **82** (1989) 362.
- [7] J. U. Brackbill and D. C. Barnes, The Effect of Nonzero $\text{div}(\mathbf{B})$ on the Numerical Solution of the Magnetohydrodynamic Equations, *J. Comp. Phys.* **35** (1980) 426.
- [8] M. Brio and C.C. Wu. An Upwind Differencing Scheme for the Equations of Ideal Magnetohydrodynamics. *J. Comp. Phys.* **75** (1988), 400.
- [9] P. Colella, Multidimensional Upwind Methods for Hyperbolic Conservation Laws, *J. Comput. Phys.* **87** (1990) 171.
- [10] W. Dai and P. R. Woodward, An Approximate Riemann Solver for Ideal Magnetohydrodynamics, *J. Comput. Phys.* 111 (1994) 354.

- [11] W. Dai and P. R. Woodward, Extension of the Piecewise Parabolic Method to Multidimensional Ideal Magnetohydrodynamics. *J. Comput. Phys.* **115** (1994), 485.
- [12] A. Dedner, F. Kemm, D. Kröner, C.-D. Munz, T. Schnitzer, and M. Wesenberg, Hyperbolic Divergence Cleaning for the MHD Equations, *J. Comp. Phys* 175 (2002) 645.
- [13] C. R. Evans and J. F. Hawley, Simulation of Magnetohydrodynamic Flows: A Constrained Transport Method, *Astrophys. J.* **332** (1988) 659.
- [14] S. A. Falle, Rarefaction Shocks, Shock Errors, and Low Order of Accuracy in ZEUS, *Astrophys. J.* **577** (2002), L123.
- [15] S. K. Godunov, The Symmetric Form of Magnetohydrodynamics Equation, *Numer. Methods Mech. Contin. Media* **1** (1972) 26.
- [16] T. I. Gombosi, K. G. Powell, and D. L. DeZeeuw, Axisymmetric Modeling of Cometary Mass Loading of an Adaptively Refined Grid: MHD Results, *J. Geophys. Res.* **99** (1994) 21, 525.
- [17] F. Harlow and J. Welch, Numerical Calculation of Time-Dependent Viscous Incompressible Flow of Fluids with Free Surfaces, *Physics of Fluids* **8** (1965) 2182.
- [18] J. F. Huang and L. Greengard, A Fast Firect Solver for Elliptic Partial Differential Equations on Adaptively Refined Meshes, *SIAM Journal on Scientific Computing.* **21**(4) (2000) 1551-1566.
- [19] M. F. Lai, A Projection Method for Reacting Flow in the Zero Mach Number Limit, Ph.D. Thesis, UC Berkeley 1993.
- [20] B. Marder, A Method for Incorporating Gauss' Law into Electromagnetic PIC Codes, *J. Comput. Phys.* **68** (1987) 48.
- [21] Miller, G. H. and Colella, P. A High-Order Eulerian Godunov Method for Elastic-Plastic Flow in Solids, *J. Comput. Phys.* **167** (2001) 131.
- [22] P. L. Roe and D. S. Balsara, Notes on the Eigensystem of MHD, *SIAM J. Appl. Math.* **56** (1996) 57.
- [23] D. Ryu, T. W. Jones, and A. Frank, Numerical Magnetohydrodynamics in Astrophysics: Algorithm and Tests for Multidimensional Flow. *Astrophys. J* **452** (1995) 785.
- [24] D. Ryu, F. Miniati, T. W. Jones, and A. Frank. A Divergence-free Upwind Code for Multidimensional Magnetohydrodynamic Flows, *Astrophys. J.* **509** (1998) 244.
- [25] F. Shu. *The Physics of Astrophysics: Gas Dynamics*. University Science Books (1992).

- [26] J. M. Stone and M. L. Norman, ZEUS2D: A Radiation Magnetohydrodynamics Code for Astrophysical Flows in Two Space Dimensions. II The Magnetohydrodynamic Algorithms and Tests, *Astrophys. J. Suppl.* **80** (1992) 791.
- [27] J. M. Stone, Personal Communication.
- [28] E.F. Toro, *Riemann Solvers and Numerical Methods for Fluid Dynamics : A Practical Introduction*. Springer-Verlag (1999).
- [29] G. Tóth, The $\text{div}(\mathbf{B})$ Constraint in Shock-Capturing Magnetohydrodynamics Codes. *J. Comp. Phys.* **161** (2000) 605.
- [30] P. R. Woodward, Piecewise Parabolic Methods for Astrophysical Fluid Dynamics, in *Astrophysical Radiation Hydrodynamics*, K.-H. Winkler and M. Norman, eds. Reidel (1986) 245.
- [31] A. L. Zachary, A. Malagoli, and P. Colella, A Higher-order Godunov Method for Multidimensional Ideal Magnetohydrodynamics, *SIAM J. Sci. Comput.* **15** (1994) 263.
- [32] A. L. Zachary and P. Colella, A Higher-order Godunov Method for the Equations of Ideal Magnetohydrodynamics, *J. Comput. Phys.* **99** (1992) 341.

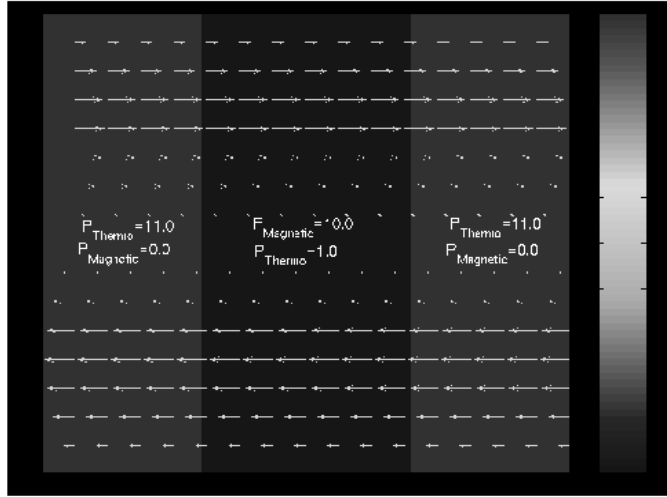


Fig. 6. Grid-aligned flux tube initial conditions. Vectors indicate the velocity field, while colors indicate the gas pressure. There are two regions: one magnetized, the other not. The entire domain is initially in total (magnetic plus thermal) pressure balance. A velocity perturbation of 1% of the Alfvén speed is applied to the entire domain, causing the tube to oscillate.

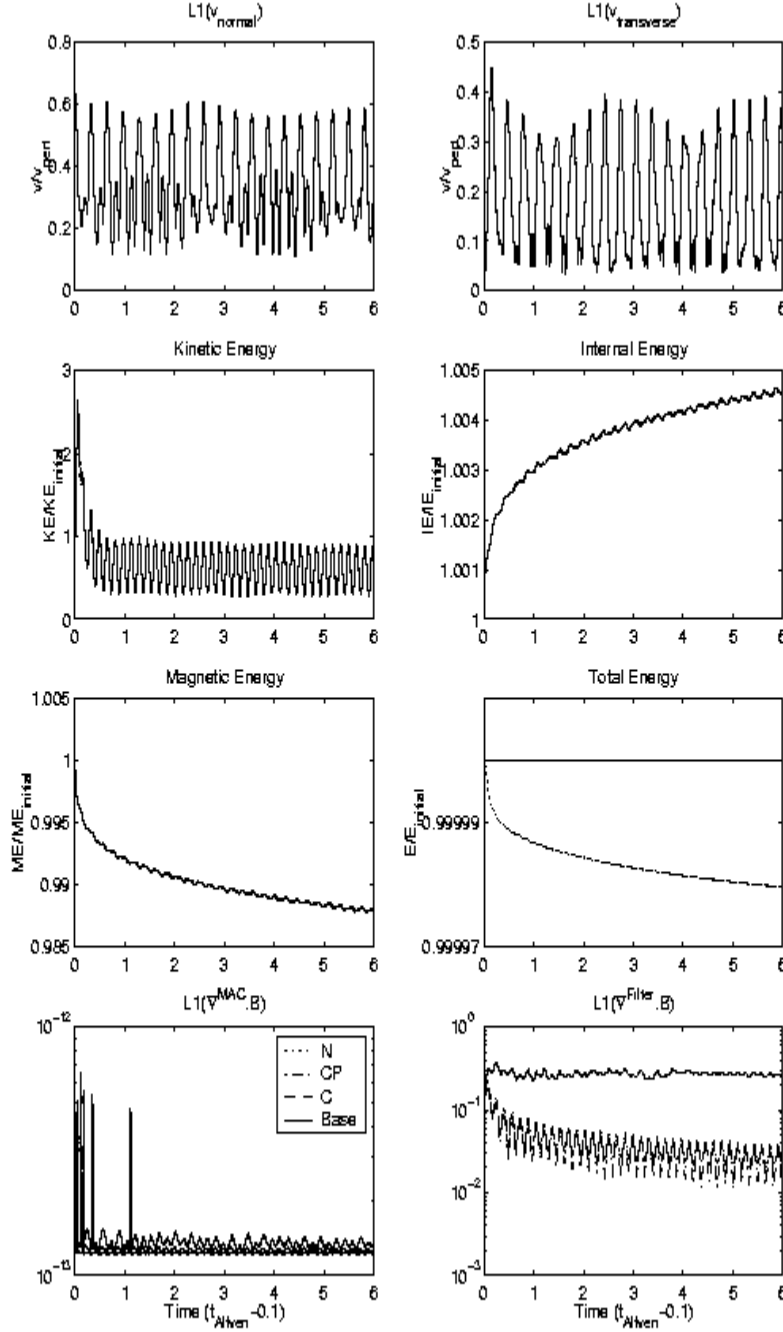


Fig. 7. Grid-aligned flux tube results for codes solving the ideal MHD equations. We use L^1 norms of velocities and monopole charge densities, plus grid-summed energies, to follow the evolution. The velocities are normalized to the initial perturbation velocity, $0.01c_A \simeq 0.045$. Energies are normalized to their initial values. The two measures of monopole charge density use different discretizations: ∇^{MAC} corresponds to the MAC divergence of the stars at cell-edges, while ∇^{Filter} corresponds to a divergence of cell-centered fields consistent with the filter. (See Equation 47.)

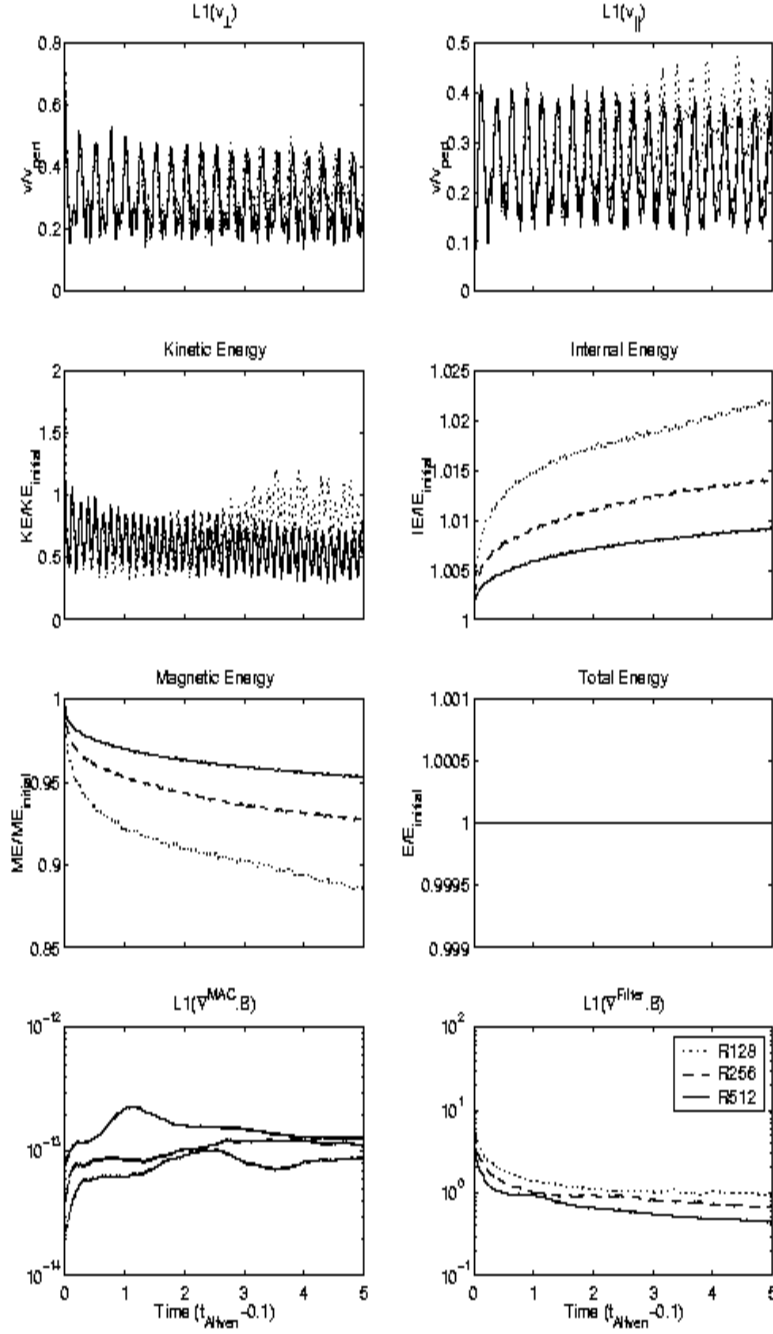


Fig. 8. Inclined flux tube results for 128, 256, and 512 cells in each direction. These results are from an ideal MHD code using conservative filtering with a coefficient of 0.0078125. The quantities shown are the same as in Figure 7.

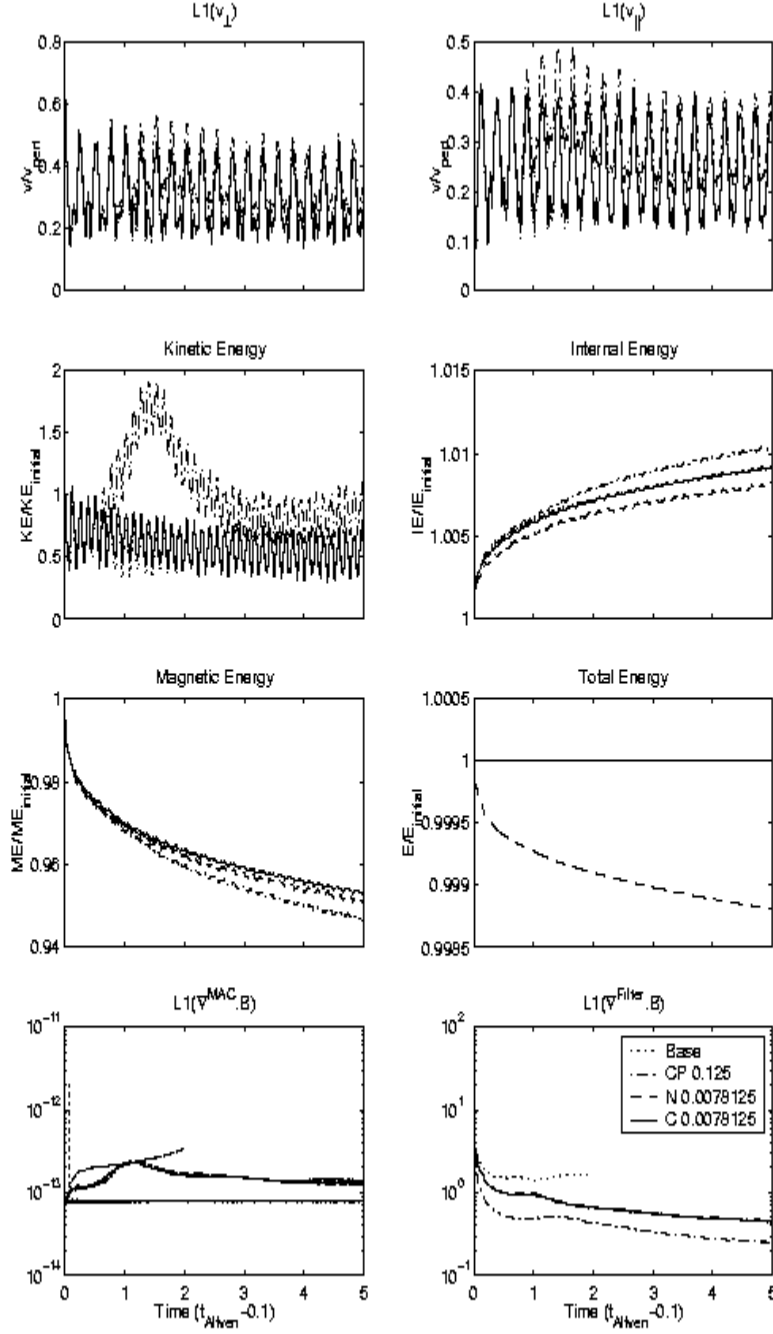


Fig. 9. Inclined flux tube results for codes solving the ideal MHD equations. The base code uses a MAC projection alone, while the others use conservative (C) and non-conservative (N) filter types, and possibly an approximate projection (P). The numbers after the filter type give the value of the filtering coefficient used. Note the rise in kinetic energy in the code with filtering coefficient $C = 0.125$, and the crash of the base ($C = 0$) code at about $t = 3.7$. The intermediate value of the filtering coefficient shown gives good results.